Experimental Measurement of Stationary SS 304, SS 316L and 8630 GTA Weld Pool Surface Temperatures

High-resolution, molten weld pool surface temperature maps are obtained for stationary GTA welds on thick plate

BY H. G. KRAUS

ABSTRACT. The optical spectral radiometric/laser reflectance experimental method, previously developed by this author, was extended to obtain high-resolution surface temperature maps of stationary GTA molten weld pools using thick-plate SS 304, SS 316L, and 8630 steel. This involved making measurements of the weld pool dome (*i.e.*, topology) and further modifications to the basic method to account for the non-flat weld pool surfaces that occur. Increasing the welding current from 50 to 200 A resulted in peak pool surface temperatures from 1950° to 2400°C for the SS 304. At a constant welding current of 150 A, the SS 304 and various heats of SS 316L and 8630 resulted in peak weld pool temperatures from 2300° to 2700°C. Temperature contour plots of all the welds made are given. Surface temperature maps are classified into types that are believed to be indicative of the convective circulation patterns present in the weld pools.

Introduction

The optical spectral radiometric/laser reflectance method, previously developed by this author (Refs. 1, 2), has been extended in order to obtain noninvasive, stationary, thick-plate gas tungsten arc (GTA), high-resolution, weld pool surface temperature maps for 304 and 316L stainless steel and 8630 medium-carbon steel. This involved making measurements of the weld pool dome (*i.e.*, topology) and further modifications of the basic method to account for the non-flat weld pool surfaces that occur. Details of this procedure, as it is different and improved from previous work, are presented below.

The purpose of this and past research (Refs. 3, 4) is to build a database for verification and further development of theoretical thermal models of weld pools using various welding conditions and different materials. This database now includes stationary and moving welding torch conditions. Previous measurements, reported in Refs. 3 and 4, were made using thin-plate SS 304 for two different welding power sources. The effect of varying welding power as well as torch translation speed were studied. Maximum weld pool temperatures showed dependencies on these parameters, as well as on which welding power source was used. The weld pool surface temperature measurements made here varied welding power from 50 to 200 A using SS 304 to investigate the effect of current on the pool temperatures. Different heats of SS 316L and 8630 were used to study the effects of minor alloying elements, such as cerium, silicon and sulfur, on weld pool surface temperatures. These were chosen to aid in assessing the well-known effect of surface tension-induced, centrally inward or outward pool surface circulation patterns on pool surface temperatures. Future plans are then to add to these measurements by including thick-plate moving welding torch measurements on SS 304, as well as sulfur- and selenium-doped SS 304. The former would include the effects of power and translation speed, while the latter would investigate surface tension effects. However, in order to accurately make such measurements, an experimental method to map the weld pool surface topology, at the same instant the temperature measurements are being made, needs to be developed.

KEY WORDS

Experimental Measure
GTA Weld Pools
Weld Pool Surface
Surface Temperatures
Stationary Weld Pool
SS 304/SS 316L/8630
Spectral Radiometric
Laser Reflectance
Temperature Contours
Surface Topology

Review

Several other methods have been used to obtain weld pool surface temperature measurements. Most of them have been reviewed elsewhere (Refs. 2, 3). They may be summarized by stating that they are either low-resolution spot temperature measurements or uncalibrated infrared emission map measurements. There is one additional significant work, by Sundell, *et al.* (Ref. 5), that needs to be identified. This report is an extensive investigation into the effects of minor alloying elements on GTA weld penetration. Spot weld pool surface temperature measurements were reported, as well as extensive molten metal surface tension data for AISI 8630 low-alloy steel, SS 316L, and Inconel 718. These temperature measurements were made for translating welds using tungsten-rhenium thermocouples inserted from the underside of the workpiece in holes drilled to within 0.38 mm (0.015 in.) from the top surface at the center and both sides of the weld. Centerline surface temperatures were reported for the point at which the thermocouple protruded through the surface due to arc pressure weld pool depression. It was not known that the location at which this occurred was ever coincident with the maximum weld pool temperature, and thus may not have recorded true peak temperature. In addition, the presence of the thermocouple in the

H. G. KRAUS is Senior Engineering Specialist at Idaho National Engineering Laboratory, EG&G Idaho, Inc., Idaho Falls, Idaho.
Paper presented at the 69th Annual AWS Meeting, held April 17-22, 1988, in New Orleans, La.

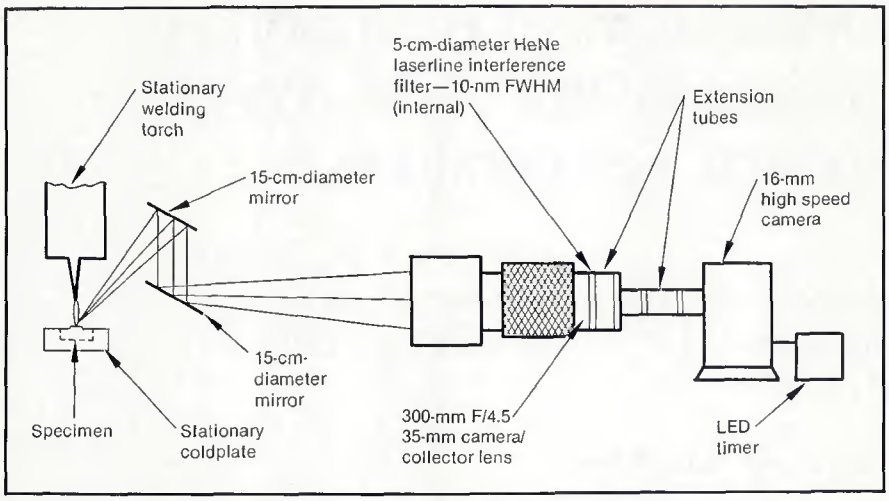

Fig. 1—Schematic for weld pool spectral directional emissive power experiment

center of the weld pool causes a loading error in the weld pool temperatures, due to altered overall pool thermophysical properties and impediment of weld pool convective circulation. There is a potential for recording erroneously low temperature values with such a method. A noninvasive weld pool surface temperature measurement method, as used here, has many advantages over previous methods, described below.

Experimental Procedure

The original development of the optical spectral radiometric/laser reflectance measurement method is described elsewhere (Ref. 2). The basis for the method is the following equation:

$$T=C_2/\lambda\ \ell n\left[1+\frac{(2C_1\cos\beta)\epsilon'_\lambda(\lambda,\beta,T)}{\lambda^5\, e_\lambda'\,(\lambda,\beta,T)}\right] \quad (1)$$

which is derived from Planck's blackbody spectral distribution of emissive power, the definition of spectral directional emissivity, and Lambert's cosine law of diffuse emitters (see Ref. 6 for definitions). In Equation 1, ϵ'_λ is the spectral directional emissivity, e'_λ is the spectral directional emissive power, λ is wavelength, β is the angle from the normal vector to a surface, and C_1 and C_2 are constants (defined in Ref. 6). Note that in order to find the temperature at a point on a flat weld pool surface, only the spectral directional emissive power and the spectral directional emissivity must be measured at a specific wavelength and a specific angle. The smaller the point or spot on the weld pool, the better the temperature resolution. However, stationary weld pool surfaces on thick plates, as investigated here, are not flat as in previous work (Refs. 2–4), so the weld pool topology must be measured in order to properly define the variation of β across the weld pool surface.

Figure 1 shows the experimental configuration for determining the spectral, directional emissive power of the weld pool. High-speed cinematography was used to photograph the weld pool thermal emissions, through a helium-neon (HeNe) laserline interference filter, to obtain a spectral measurement. The filming interval extended from steady state conditions through welding power shutoff. The film image of interest is that obtained immediately after arc emissions cease, so as to have a spectral emission image of the weld pool in the absence of arc plasma emissions.

The welds were made with the torch held stationary over the specimen. The specimen was mounted in a specially designed cold plate to provide well-defined boundary conditions for use in theoretical models. This cold plate is comprised of two plates as shown in Fig. 2. The bottom plate has a cavity machined in it, open on top, through which water is circulated via inlet and outlet taps on the side. It is sealed by means of an O-ring to the top plate, which is solid on its bottom. The top plate also has a cavity machined in its top surface, although smaller than the bottom plate cavity, into which specimens can be placed. The cold plate is grounded at the center of each of its four lateral faces to provide symmetry of the induced magnetic field in the specimen. The specimen thermal boundary conditions were thus defined by constant temperature on its bottom and lateral faces. The top surface was subject to convective and radiative heat loss. All welds were made in the center of 4- × 4-cm (1.6- × 1.6-in.) specimens that were held securely in the top plate cavity by eight bolts, two on each face of the lateral perimeter.

Filming speed was a critical factor in obtaining useful information with respect to film image density, and is discussed in detail in Ref. 2. Filming speed was accurately calculated using LED timing marks recorded on the edge of the film during all runs, as shown in Fig. 1.

Controlled processing is used to develop the film, and spectral sensitometry via a neutral-density step wedge (using also the same HeNe laserline filter) provides recorded density (D) as a function of exposure (E). Figure 3 shows the film sensitometry curves (*i.e.,* calibration curves) for the stationary weld run reported below. Calibration strips were run at the beginning and end (head and tail) of the processing of the roll of film to assess any variation in processing during that time interval. The film images, having a scale near 1:1.3, were microdigitized for density using a 60 μm square aperture. The film used was 16-mm high-speed red-sensitive (Kodak 2484) film, which closely matched the laserline filter peak transmission centered at 632.8 nm (the HeNe laser emission wavelength).

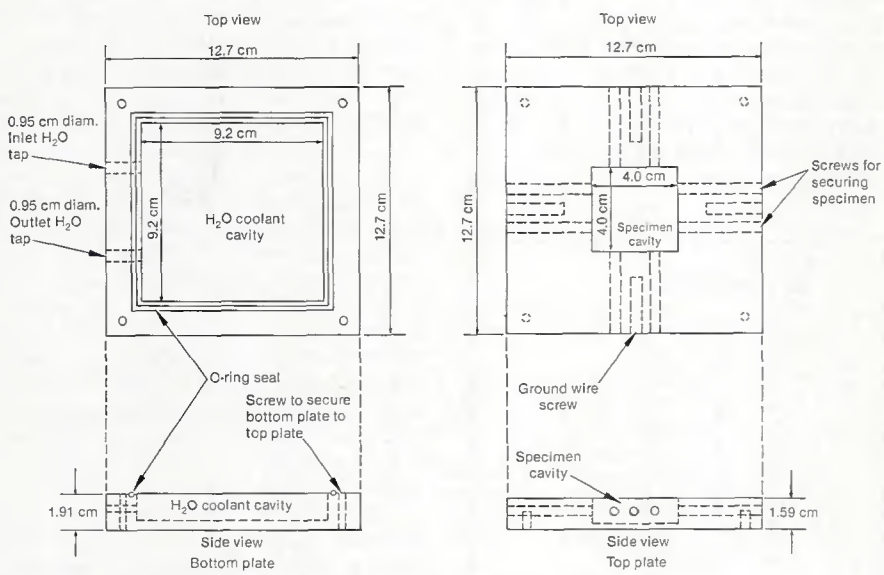

Fig. 2—Drawing of cold plate used for stationary thick-plate welds

Additional detail with respect to film processing and reciprocity effects are discussed in Ref. 2. Film density at each pixel was linearly interpolated between the head and the tail of the film, based on the film footage number of the weld pool image used. Noise in the images caused by film grain clumping was filtered out, using a two-dimensional digital convolution filter.

The sensitometric curves provide a relative exposure response of the film. To obtain an absolute measurement of spectral directional emissive power from the film density data for use in Equation 1, an absolute reference or calibration point must be defined for the sensitometric data. This was accomplished for the nearly flat weld pools (Ref. 2) by matching the actual weld pool perimeter to a particular film image constant density contour at the phase front of the weld pool, where the temperature (melting temperature of the metal) and the spectral directional emissivity are known. This temperature was assumed to be the average of the solidus and the liquidus temperatures for the alloy. However, for the non-flat surfaces of these stationary weld pools, β is not constant around the perimeter of the weld pool, and a single calibration point must be chosen for a unique temperature/spectral directional emissivity/β combination. This point chosen was the right-most edge of the pool, as recorded on film. The appropriate value of β is the angle between the normal to the weld pool surface and the optical train viewing angle. Calibration otherwise proceeds as in previous work by matching the minimum weld pool density contour to the actual measured weld pool boundary. The spectral directional emissivity data and the metal phase change temperature may then be combined with the calibration point to calculate the known spectral directional emissive power. The associated film image recorded intensity, $I = 1/(10^E \Delta t)$ (see Fig. 3), is then equated to the product of a density calibration factor ρ, called the "wavelength constant," and this known value of e'_λ. From this product, ρ can be determined and has been shown to be a system parameter that gives a relative indication of the radiation collection/recording efficiency at a given wavelength for the spectral directional emissive power, and has units the same as for wavelength. It depends on many things, including film type, filming speed, film processing, mirror reflectivities, and camera lens and laserline filter transmission characteristics. However, it remains fixed for any particular system and a given film image. Therefore, density values at all film image pixels are then converted to absolute spectral directional emissive power values using the relationship $e'_\lambda = I/\rho$. Reference 2 contains additional details.

Calculation of the film image pixel temperatures through Equation 1, as well as the above film calibration, require that the geometry of the surface of the weld pool be measured so that the angle for which the emissions are being observed can be determined. The angle of interest is that between the optical train observation angle and the normal vector to the surface at the pixel location. The weld pool topology was determined using the experimental setup shown in Fig. 4. The optical axis was aligned at the same level as the plane of the top surface of the cold plate, which was coincident with the top surface of the specimen. Various camera lens apertures were used to enable filming of the top edge of the molten pool. The laserline filter was used to aid in rejecting enough of the arc emissions to record weld pool emissions. Typical weld pool profile measurements are shown and discussed in the Results section of the paper.

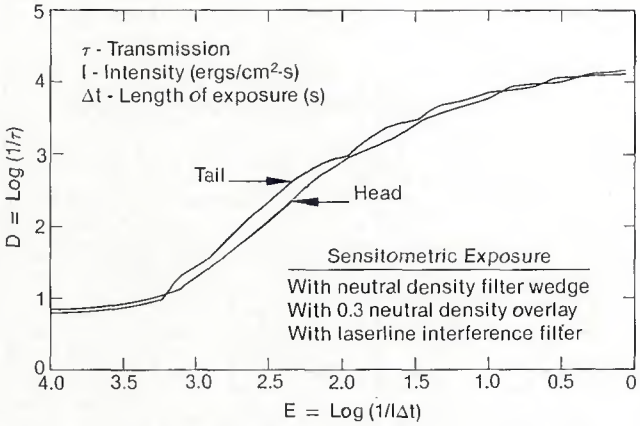

Fig. 3 — Kodak 2484 high-speed film microdensitometer spectral sensitometry curves (film calibration), beginning and end of film roll

The spectral directional emissivity of thin-plate SS 304 weld pools was measured as a function of location and time after arc (and thus temperature) shutoff in previous research (Refs. 2 and 3). This was done by reflecting a focused helium-neon laser beam off of the weld pool and relating the spectral directional reflectivity to the spectral directional emissivity via Kirchoff's law, as (Ref. 6):

$$\epsilon'_\lambda(\lambda,\beta,T) = 1 - \rho'_\lambda(\lambda,\beta,T) \qquad (2)$$

In this equation, ϵ'_λ is the spectral directional emissivity, and ρ'_λ is the spectral directional reflectivity. The present work used nearly the same experimental configuration as before, and is shown in Fig. 5. The integrating sphere/radiometer calibration procedure was identical to that used before (Ref. 2). However, the experimental procedure differed somewhat, in that the reflection measurements were performed with the welding arc on. The spectral directional reflectivity was then determined by means of the calibration curve data relationship (Equation 12 of Ref. 2). The reflectivity oscilloscope trace used was that for the laser-on-weld-pool-reflected measurements having the laser-off-weld-pool/arc emission signal subtracted. The reference oscilloscope trace used was the direct laser beam to integrating sphere signal. The laserline focusing lens and the laserline interference filter remained in place for all measurements. The location of the beam on the weld pool surface then allows the association with temperature at that location to be made. The non-flat weld pool surface topology of the stationary welds required an assessment of the dependence of ϵ'_λ on β, as well. Results for the various metals used in these experiments are given below.

Weld pool temperatures are finally determined through Equation 1 by using

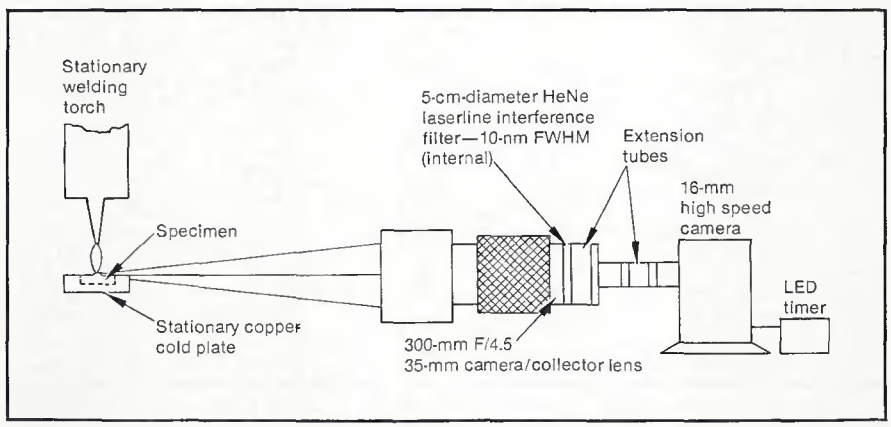

Fig. 4 — Schematic for making film-based measurements of stationary weld pool profiles

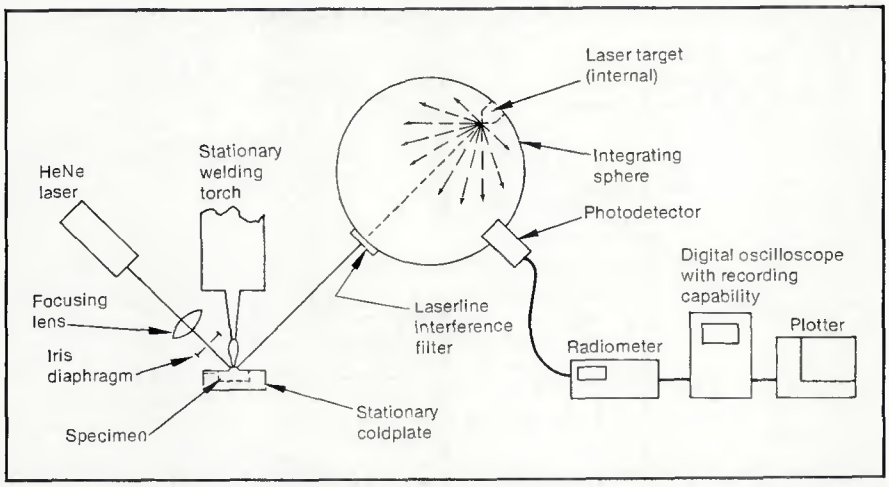

Fig. 5 – Schematic for weld pool spectral directional emissivity experiment

the spectral directional emissive power, spectral directional emissivity, and weld pool topology/β data corresponding to each pixel on the 16-mm film frame. Note that Equation 1 requires the measurement of temperature at a pixel to be made using the same value of β for both the emissive power and the emissivity measurements at a pixel. Temperatures below the phase change temperature are not determined. If the emissivity is temperature dependent, a trial-and-error procedure is required in Equation 1 to determine each pixel temperature, for it is not known *a priori*.

Results and Discussion

The first four columns of Table 1 summarize the stationary weld pool surface temperature runs made. Four welds on a single heat of SS 304 were used to study the effect of welding current (or welding power), from 50 to 200 A on weld pool surface temperatures. Welds were made on three heats of SS 316L and four heats of 8630 steel at 150 A, and are to be compared to each other and to the 150-A SS 304 case. The compositions of these metals are given in Tables 2 and 3. A ⅛-in.-diameter (3.2-mm), 30-deg cone angle, 2% thoriated, tungsten electrode was used. The optical axis angle with the plane of the top surface of the workpiece was 48 deg. The preweld electrode gap was 2.0 mm (0.08 in.). The argon cover gas had a flow rate of 18 cfh (8.5 L/min). The cold plate and specimens were initially at the H_2O coolant temperature of 15°C (59°F). An Astro Arc Astromatic E-300-PC welding unit was used for all welds. After striking the arc, weld pool sizes, and presumably weld pool temperatures, stabilize in several seconds (see also Ref. 5), allowing quasi-steady-state conditions to be reached. Even so, all welds were run for 25 s before the arc shutdown or welding unit shutoff sequence was initiated. Upon shutting the unit off, while the high-speed camera was running, the resulting arc decay times were 3 to 11 ms. Actual arc shutoff times for welding currents from 50 to 250 A were initially measured by filming the event with the high-speed camera running at 1000 fps. Results of these data are reported in Fig. 6 to the nearest 0.5 ms. The welds reported in Table 1 were filmed at 280 fps and maximum temperature results for the welds are reported for the first frame where arc emissions are not present in the film image. The times from Fig. 6 and Table 1 do not necessarily exactly match because the time between frames for the latter is 3.57 ms. However, these arc shutoff times and those of Ref. 4 are an order of magnitude faster than those obtained in previous research, in which a Miller Synchrowave 300 welding power source (Refs. 2, 3) was used. It was hoped that these new measurements would more closely represent temperatures that exist when the arc is on. An experimental data-based estimate of the change in maximum weld pool temperature during arc shutoff will be presented later.

Figure 7A shows the weld pool geometric profile at the end of arc shutoff for Case 3, which is the base case of the 150 A runs. This profile is typical of those measured for all cases except for the 8630/3040 heat. Only the height of the dome and its diameter vary significantly from case to case, and these are reported in Table 1. Results were highly repeatable. Central weld pool depression was checked for but not observed in the 1000 fps welding arc shutoff time runs, where the viewing angle was similar to that of Fig. 1. Lin and Eagar (Ref. 7) have also reported experimental results for stationary welds made on steel showing that pool surface depression was negligible for welding currents less than 200 A. The accuracy of the profile measurements reported here was estimated to be ±0.025 mm (0.001 in.). Note that the central region of the pool approaches

Table 1—Conditions Summary for SS 304, SS 316, and 8630 Thick-Plate GTA Stationary Weld Pool Surface Temperature Measurement Runs, with Maximum Temperature Results

Case No.	Material/ Heat Number[a]	Voltage, (V)	Current, (A)	Time after Beginning of Emissions Decay, ms[b]	Maximum Observed Temperature, K (°C)	Temperature Topology Type	Weld Pool Diameter, (mm)	Weld Pool Dome Height, (mm)
1	SS 304/1	10.1	50	<3.6	2220 (1947)	I-B	3.0	0.16
2	Ss 304/1	13.2	100	3.6–7.2	2433 (2160)	II-B	5.8	0.41
3	SS 304/1	15.1	150	3.6–7.2	2699 (2426)	I-B	8.8	0.51
4	SS 304/1	15.1	200	7.2–10.8	2488 (2215)	III	11.3	0.75
5	SS 316L/J	15.1	150	3.6–7.2	2612 (2339)	I-B	11.9	0.24
6	SS 316L/L	14.7	150	3.6–7.2	2591 (2318)	II-B	8.6	0.50
7	SS 316L/M	15.1	150	3.6–7.2	2839 (2566)	I-A	8.8	0.51
8	8630/3037	15.5	150	3.6–7.2	2981 (2708)	I-A	8.8	0.51
9	8630/3040	15.5	150	3.6–7.2	2783 (2510)	I-B	9.0	0.85[c]
10	8630/3043	15.5	150	3.6–7.2	2636 (2553)	I-A/II	9.2	0.53
11	8630/3046	15.0	150	3.6–7.2	2669 (2396)	I-A	8.8	0.51

(a) The heat numbers for SS 316 and 8630 are those referred to in Ref. 5. All SS specimens were 4 × 4 × 1.25 cm, and the 8630 specimens were 4 × 4 × 0.89 cm.
(b) In all cases the, welding machine was run for 25 s before arc shutoff, which produced a fixed weld pool size for more than 15 s. Coldplate H_2O coolant temperature was 288 K (15°C).
(c) This peak weld pool dome height does not occur in the center of the weld, as is true for the other welds; the dome was skewed, being lower on one side than the other.

Table 2—Chemical Composition of AISI SS 304 and SS 316L Thick Plates

Element	SS 316L, Heat J, wt-%	SS 316L, Heat L, wt-%	SS 316L, Heat M, wt-%	SS 304, wt-%
C	0.011	0.015	0.012	0.1
Co	–	0.09	0.16	N/A
Cr	17.15	16.45	16.50	18.1
Cu	–	0.32	0.18	0.33
Fe	bal.	bal.	bal.	bal.
Mn	1.59	1.84	1.67	1.60
Mo	2.73	2.10	2.06	0.31
N	0.105	0.073	0.080	N/A
Ni	12.65	10.34	10.18	8.4
P	0.022	0.030	0.030	0.040
S	0.001	0.003	0.013	0.022
Si	0.60	0.40	0.62	0.69
V	–	–	–	0.48

Table 3—Chemical Composition of AISI 8630 Steel Thick Plate Heats

Element	Heat 3037[b], wt-%	Heat 3040, wt-%	Heat 3043, wt-%	Heat 3046, wt-%
C	0.33	0.33	0.32	0.32
Ce[a]	N/A	N/A	0.010	0.015
Cr	0.50	0.51	0.52	0.53
Fe	bal.	bal.	bal.	bal.
Mn	0.77	0.81	0.81	0.82
Mo	0.20	0.20	0.20	0.20
Ni	0.56	0.58	0.52	0.53
P	0.012	0.010	0.007	0.005
S[a]	0.007	0.020	0.004	0.017
Si[a]	0.13	0.49	0.14	0.48

(a) Major heat differences.
(b) Heats are referred to in Ref. 5 by the last digit only.

being flat on top. As previously reported, these measurements correspond to the time for which arc emissions have ceased. This is when it is possible to measure temperatures by this method. Complete weld pool topology for these welds was closely represented by assuming that the profiles were axisymmetric about the central axis through the length of the electrode. Measurements of these profiles under quasi-steady-state conditions with the arc on show the dome is typically more curved than flattened on top, as shown in Fig. 7A. This profile changes continuously during arc decay, and the central region continues to oscillate up and down long after the arc is extinguished, particularly in some of the 150 A and 200 A cases. The magnitude of this oscillation varies from nearly imperceptible to a couple tenths of a mm, depending on the welding current and material used. This effect is believed to be due to removal of the arc-induced pressure on the top surface of the weld pool. It is also controlled by changing surface tension forces as the weld pool cools slightly during arc decay in the localized region of the arc impingement point on the weld pool. The 8630/3040 heat, however, does not form a steady weld pool surface during quasi-steady-state welding conditions. Instead, it oscillates from one side to the other and is asymmetrical in nature. Measurements of its emissive power and of its profile were taken broadside to this oscillation and had to be filmed during arc decay when oscillation of the weld pool peak height was to the right, as shown in Fig. 7B, so that the two measurements corresponded in geometric configuration—basically a hit-and-miss proposition. In this case, the pool remained strongly dome-shaped throughout arc decay. The complete topology of this weld pool was generated by using linear angular geometric interpolation from the right-half to the left-half radial profiles. These profile measurements were otherwise also very repeatable.

Past research results showed that the spectral directional emissivity has a very small dependence on temperature for thin-plate SS 304 (Ref. 2) in the temperature range from 1900 K to over 2600 K. Further investigation into this possibility for the metals shown in Table 1 also revealed no significant temperature dependencies. This was assessed by moving the laser beam around the pool and measuring any differences in reflected laser beam intensities. Angular dependencies were also investigated, and the Table 4 SS 304 results are a sample of the measurement results. Similar results were obtained for all the metals. Because these variations were small, values of several measurements made at an angle of incidence of 48 deg from normal to the weld pool surface were averaged and are given in Table 5. Table 5 values were used for all temperature calculations.

Emissive power measurements, emis-

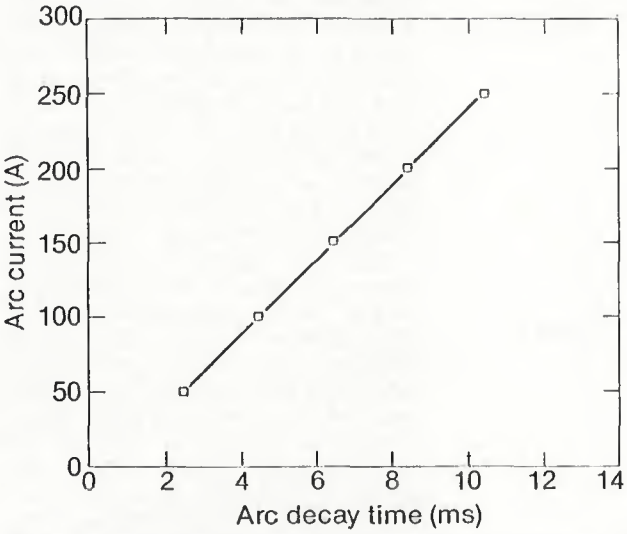

Fig. 6—Arc extinguish times for GTA welds as a function of current for 2-mm gap, 15 V, 18 cfpm argon shielding gas, 1.25-cm-thick SS 304, using Astro Arc Astromatic E-300-PC welding unit

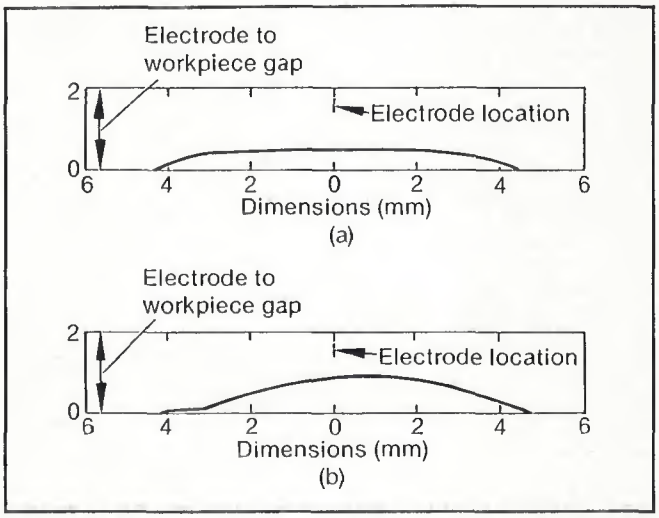

Fig. 7—Weld pool profiles in a plane perpendicular to top surface of specimen and containing central axis through the length of the electrode: A—SS 304, 150 A (Case 3 of Table 1); B—8630/3040, 150 A (Case 9 of Table 1)

Table 4—Experimental ϵ_λ' Measurements on Thick Plate AISI SS 304, Various Values of β

β	ϵ_λ'[(a)]
36	0.43
36	0.42
42	0.41
42	0.41
48	0.42
48	0.40
54	0.40
54	0.40
60	0.42
60	0.41
66	0.42
66	0.41

(a) Experimental uncertaintly of these values is ± 0.02.

Table 5—Average Experimental ϵ_λ' Measurements on Thick Plate AISI SS 304, SS316L and 8630 Heats[(a)]

Material	Average ϵ_λ'[(b)]
SS 304	0.41
SS 316 L/J	0.39
SS 316 L/L	0.48
SS 316 L/M	0.54
8630/3037	0.44
8630/3040	0.45
8630/3043	0.41
8630/3046	0.44

(a) Experimental uncertainty of these values of ± 0.02. Typical range of data was 0.01 to 0.03.
(b) These measurements were at β = 48° and were used for all values of β, as experimental investigations for SS 304 showed little variation with β.

sivity measurements, and weld pool topology measurements were combined to enable film image pixel temperatures to be determined. Temperature results are given in Table 1 and Figs. 8 through 20. An analysis of the sources of experimental and processing errors involved in these absolute temperature measurements has been performed in a manner similar to that given in Ref. 2 and is believed to be ±2.5%.

Table 1 peak weld pool temperature results range from 1950° to 2700°C[1]. The 150 A cases average 2450°C for the peak temperature. These are, in general, significantly above the translating electron beam 304 stainless steel peak weld pool temperature results of 2100°C (2373 K) by Shauer, *et al.* (Ref. 8); the 2000°C (2273 K) peak stationary 304 stainless steel weld pool measurements by Giedt, *et al.* (Ref. 9); and the vaporization theory-based calculations of 2010°C (2283 K) for 10% of the workpiece input energy going into metal vaporization in stainless steels by Block-Bolton and Eagar (Ref. 10). Block-Bolton and Eagar do, however, report a predicted peak temperature of 2520°C (2793 K) for the upper bound case of 100% of the workpiece energy going into metal vaporization. This, unfortunately is physically unrealistic. The buried thermocouple measurements by Sundell, *et al.* (Ref. 5) showed peak temperatures of 1810°C (2083 K) for GTA welds on SS 304, ¾-in.-thick (19-mm) plate using 250 A and a 3 ipm (76 mm/min) torch translation speed. It is believed that the high temperatures recorded in the stationary welds of Table 1 are partially the result of the high-resolution noninvasive capabilities of this method and partially the result of having the long 25-s duration for weld pool and specimen heatup, with no translation, which allowed temperatures to approach maximum levels.

[1]These peak temperatures occur between the tip of the electrode and its spectral reflection off of the weld pool. Although the edge of the electrode and its reflection form sharp boundaries in the original film images, the digital-convolution noise filtering causes the sharp edges to be less distinct. This is the reason for the apparent temperature saddle between the electrode and its reflection. However, this filtering actually has an insignificant effect on the magnitude of the temperature in the central region between the electrode and its reflection, where the peak temperatures occur.

An estimate was made of the change in magnitude of the Table 1, Case 3 peak weld pool temperature during arc decay. Maximum weld pool surface temperature data from five successive film frames, beginning with the end of arc shutoff, are plotted in Fig. 8. These data were used to extrapolate back in time to the beginning of arc decay, assuming that the energy was removed from the electrode at a rate that is linear with time. This linear rate of decay in time is supported by the data of Fig. 6 and is believed to be due to the transistor diversion bank present in the Astro Arc welding unit. This bank is used to divert the energy away from the electrode upon sequenced or emergency shutoff. Thus, the power decay is linear rather than exponential, the latter being typical of resistance-inductance circuits. This extrapolation shows a peak temperature of 2816 K (2543°C) at the beginning of arc decay. This corresponds to a peak temperature drop of about 4.5% during arc decay. Similar analysis shows a decrease of 1.5%, 3.0% and 6.0% for the 50-, 100-, and 200-A conditions. However, those temperature decreases correspond only to the peak temperature region of the weld pool; presumably, the remainder of the weld pool cools at a slower rate during arc decay, as no movement of the weld pool boundaries has been observed during this interval.

Certainly, no maximum weld pool temperatures should have been observed that are higher than the boiling points of the alloys. The boiling points of Cr, Ni and Fe—the main elements of SS 304, SS 316L, and 8630—are 2500°, 2730°, and 3000°C, respectively. On a wt-% basis, the boiling points of these alloys may be calculated to be 2890°, 2880°, and 3000°C, respectively. In no case did the temperatures reported exceed these limits. The highest measured peak temperature of any of the welds of Table 1 was 2708°C. This was for the 150-A Case 8, where the back-extrapolation of 4.5% to the beginning of arc decay of (analogous to the 150 A weld of Case 3, Fig. 8) resulted in a peak temperature of 2830°C. This is still under the 3000°C boiling point of the 8630.

Figures 9 through 19 are the isothermal temperature plots for the welds listed in Table 1. The electrode and its reflection temperatures are fictitious, as no attempt was made to measure the spectral directional emissivity properties of the electrode. Removal of the electrode and its reflection in these plots, followed by contour fill-in, is possible. However, this was not done to avoid misrepresentation of the often complex patterns measured, since there is no way of assuring that these would represent the temperatures that actually existed. All data correspond-

Fig. 8—Maximum pool surface temperature as a function of time for SS 304, 150-A weld, starting from the initiation of arc shutdown (Case 3 of Table 1)

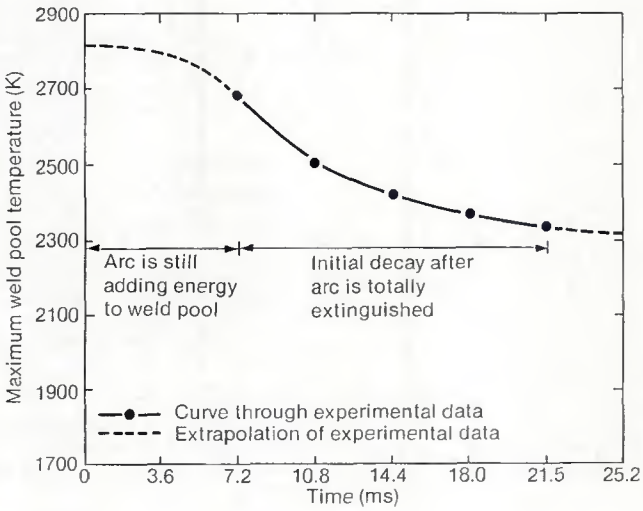

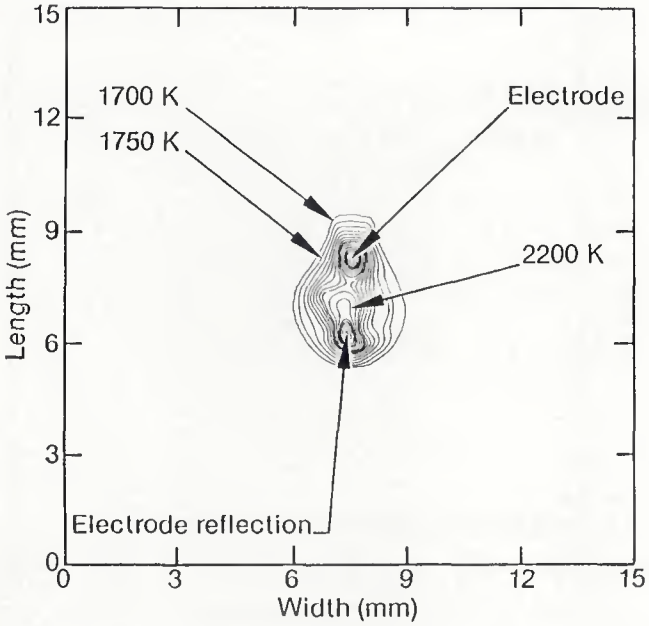

Fig. 9 — Weld pool surface isothermal temperature contours for 50-A, 10.1-V, SS 304 weld (Case 1 of Table 1)

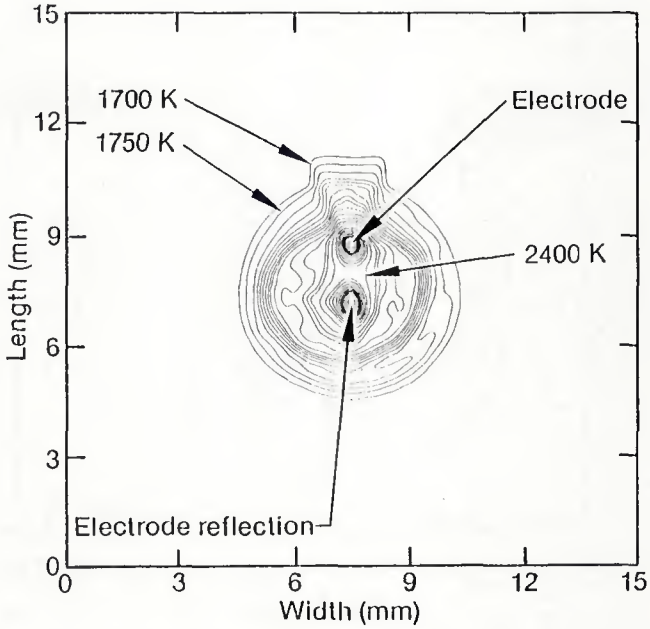

Fig. 10 — Weld pool surface isothermal temperature contours for 100-A, 13.2-V, SS 304 weld (Case 2 of Table 1)

ing to the diffuse electrode reflection off of the solid metal outside the weld pool at the bottom of these images have been removed. Straight weld pool edges are due to image clip-off when the weld boundary slightly exceeded the field of view of the high-speed camera. Temperatures below the 1700 K melting temperature of SS 304 and SS 316L, and the 1760 K (Ref. 5) of the 8630 are not shown. The images have been flattened by accounting for the optical axis angle of view and the geometric topology of the weld pools to provide a perspective directly above the weld pool center.

Figures 20A–C are plots of the temperature profiles corresponding to the cases of Table 1 grouped by alloy, for the SS 304, SS 316L and 8630 runs. The profiles are taken from left to right through the midpoint between the electrode and its spectral reflection in the weld pool. They have been classified into types, as indicated in Table 1 and Figs. 20A–C, according to their general characteristics. These types were derived, as described below, based on inferred convective circulation patterns. Types I-A and I-B have sharp central temperature peaks with no shoulders in the profile. Types II-A and II-B have central temperature peaks with shoulders at a lower or higher level on the sides of the profile. Type III has a more complicated pattern that includes a central temperature peak and multiple shoulders on the sides of the profile.

Types I-A, I-B, and II-B temperature profiles are believed to correspond to the flow patterns which have been observed previously by Heiple and Roper (Ref. 11); Heiple, Roper and Aden (Ref. 12); Burgardt and Heiple (Ref. 13); and also investigated by Sundell, *et al.* (Ref. 5). Based on the work of these authors and continuing collaborative research by this

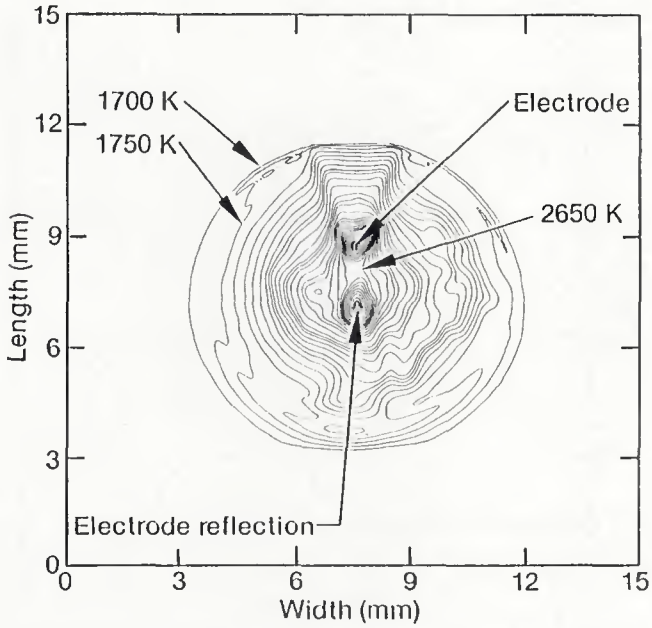

Fig. 11 — Weld pool surface isothermal temperature contours for 150-A, 15.1-V, SS 304 weld (Case 3 of Table 1)

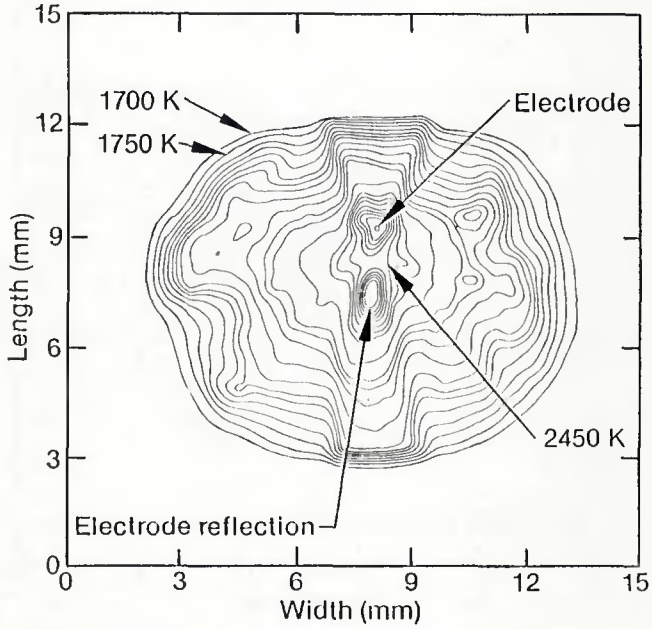

Fig. 12 — Weld pool surface isothermal temperature contours for 200-A, 15.1-V, SS 304 weld (Case 4 of Table 1)

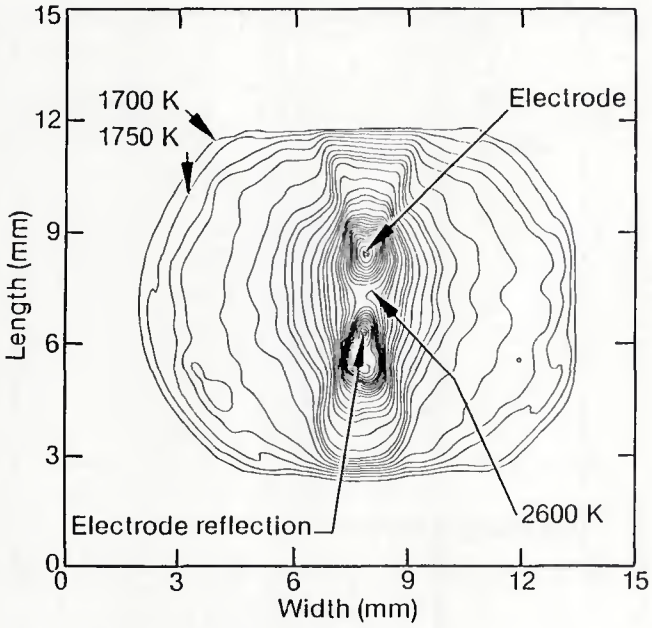

Fig. 13 — Weld pool surface isothermal temperature contours for 150-A, 15.1-V, SS 316L/J weld (Case 5 of Table 1)

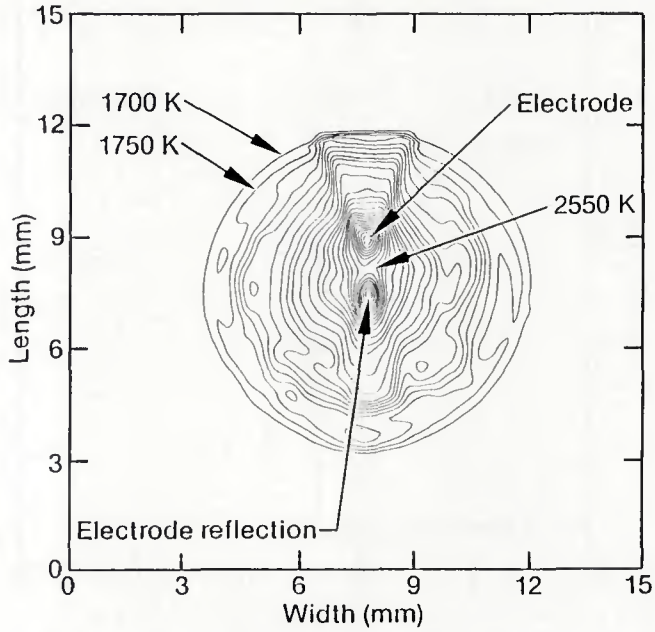

Fig. 14 — Weld pool surface isothermal temperature contours for 150-A, 14.7-V, SS 316L/L weld (Case 6 of Table 1)

author with David and Zacharia (of Ref. 14), Figs. 21A–D illustrate the primary weld pool flow patterns believed to be present when Types I or II temperature profiles exist. Of main concern are the various combinations of dominating surface tension and/or electromagnetic forces driving the weld pool convective circulation. No attempt was made to show small convection cells or vortices which might be present. The left-side figures are top views, and the right-side figures are vertical cross-sections of the weld pool circulation paths. Figures 21A and B illustrate weld pool convection patterns that are typical of Marangoni or surface tension, γ, driven flow. If $\partial\gamma/\partial T > 0$, circulation on the surface is toward the center and downward in the center interior of the weld pool, creating a narrow, deep weld pool, as in Fig. 21A. This type of surface tension temperature dependence is associated with surface active impurities (minor alloying elements) such as oxygen, sulfur, selenium and tellurium, which tend to reverse the normal $\partial\gamma/\partial T < 0$ of pure metals and alloys (Refs. 5, 15). If electromagnetic forces are significant, they enhance the inward surface circulation. If $\partial\gamma/\partial T < 0$ and electromagnetic forces are insignificant, circulation on the surface is away from the center, forming a shallow, broad weld pool, as in Fig. 21B. Two possibilities exist for the cells to divide radially. While the surface tension is nearly always temperature dependent for molten metals, it is the presence of what will be referred to as the critical or transition temperature that results in the first possibility. When $\partial\gamma/\partial T > 0$ for temperatures just above melting, it will usually remain so as temperature increases, up to some critical temperature where γ peaks in value. Thereafter, $\partial\gamma/\partial T < 0$ (*e.g.*, some of the

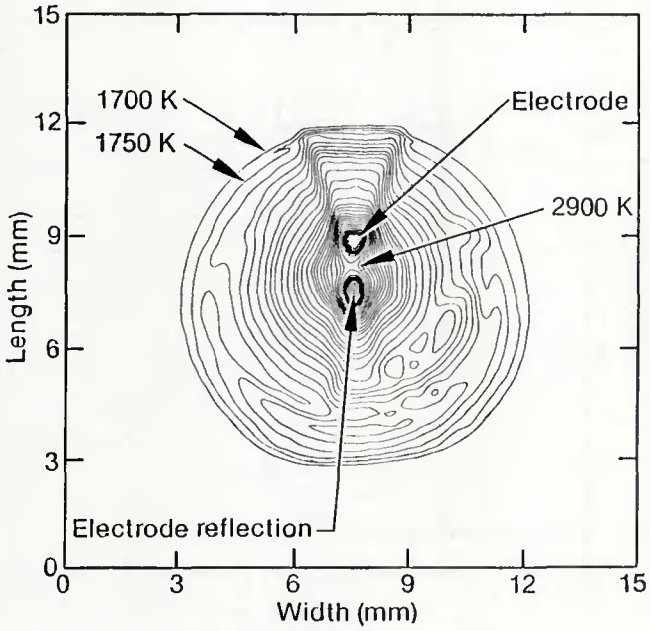

Fig. 15 — Weld pool surface isothermal temperature contours for 150-A, 15.1-V, SS 316L/M weld (Case 7 of Table 1)

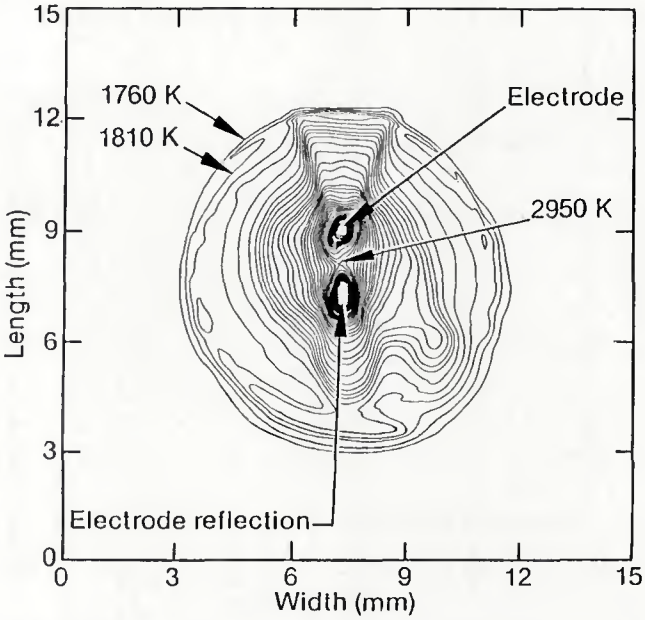

Fig. 16 — Weld pool surface isothermal temperature contours for 150-A, 15.5-V, 8630/3037 weld (Case 8 of Table 1)

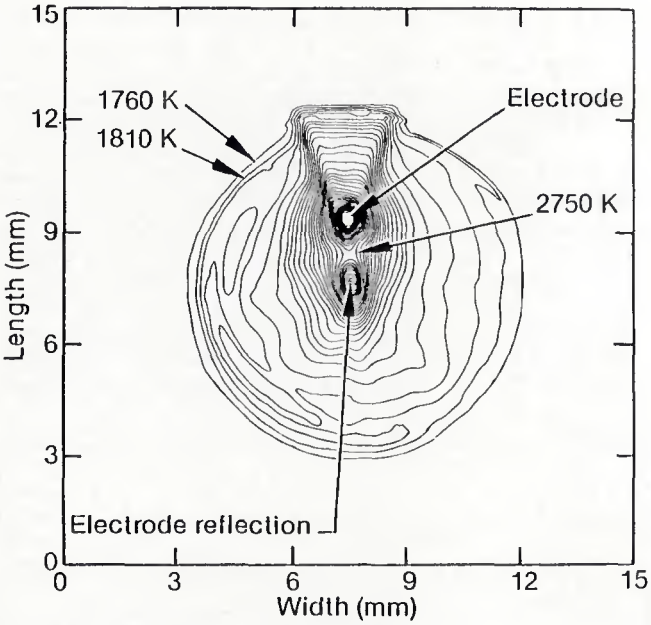

Fig. 17 — Weld pool surface isothermal temperature contours for 150-A, 15.5-V, 8630/3040 weld (Case 9 of Table 1)

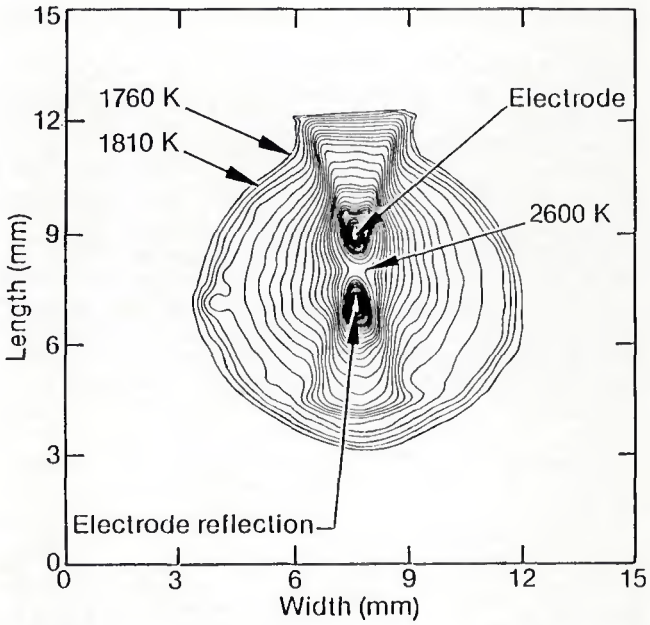

Fig. 18 — Weld pool surface isothermal temperature contours for 150-A, 15.5-V, 8630/3043 weld (Case 10 of Table 1)

8630 steel heats, Ref. 5). With $\partial\gamma/\partial T > 0$ for the lower temperature (outer) region of the weld pool and $\partial\gamma/\partial T < 0$ for the higher temperature (inner) region of the pool, opposing surface tension-driven circulation cells form, as in Fig. 21C. Reversion to Type I-A convective flow patterns would result when electromagnetic forces are dominant in the inner region. This phenomenon may also be observed at higher welding currents due to more rigorous convective mixing or entrainment of the surface active elements. This lowered concentration of surface active elements causes reversion to the pure metal or alloy $\partial\gamma/\partial T < 0$. In this scenario, either Type I-A or Type II-A could revert to either Type I-B or II-B (explained below), depending on the relative magnitudes of the surface tension and electromagnetic forces. The second possibility exists if $\partial\gamma/\partial T < 0$ and electromagnetic forces are significant. Again, a double-celled circulation pattern, as depicted in Fig. 21D, will result due to the opposing directions of these forces. The shoulders present in Type II temperature profiles are believed to occur where the two convection cells meet, as illustrated in Fig. 21C and D.

The weld pool convection cell circulation patterns believed to be associated with Type III temperature profiles do not appear to have been previously identified in the context of welding. Reexamination of Fig. 12 shows multiple lobes of the temperature contours in the angular direction around the vertical axis through the center of the weld. This phenomenon was dominant only in the 200-A, SS 304 weld. Therefore, Type III temperature profiles may be uniquely associated with higher current welds. These are believed to result from multiple convection cells, as illustrated in Fig. 21E. It is possible that circulation patterns could exist with single or double cells in the radial direction, analogous to Figs. 21 A–D, with multiple cells in the angular direction. This could give rise to at least four different Type III temperature profiles based on the different combinations of significant surface tension and electromagnetic forces. More complex Type III patterns are possible. These angular-direction, multiple-cell circulation patterns may be similar to Bernard cells (Ref. 16), but driven by a different combination of forces. Bernard cells are primarily driven by surface tension and buoyancy forces, whereas these weld pool convection cells, which are known to be driven by surface tension and electromagnetic forces, may be driven by buoyancy forces as well when dealing with high welding currents and large weld pools. That is to say, since buoyancy forces account for the breakup into multiple cells in the Bernard patterns, this force may also account for the multiple cells present in the angular direction of such weld pools. Indeed, further research in this area is certainly warranted for verification and development of these ideas.

The weld pool temperature profile type classifications in Table 1 will next be examined in the context of Figs. 20A–E and relevant surface tension data. The SS 304 used for obtaining Table 1 results behaves

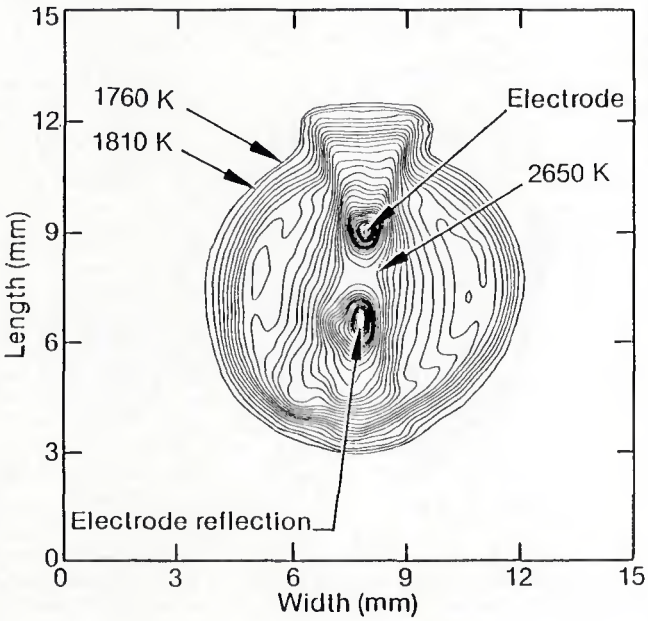

Fig. 19 — Weld pool surface isothermal temperature contours for 150-A, 15.5-V, 8630/3046 weld (Case 11 of Table 1)

in a normal fashion with respect to surface tension, *i.e.*, $\partial\gamma/\partial T < 0$. Thus, Type I-B or Type II-B temperature profiles are expected. Figure 20A shows that this is true for the 50-, 100- and 150-A cases, for which Type I-B, Type II-B and Type I-B profiles result, respectively. As discussed above, the 200-A case results in a complex Type III weld pool surface temperature pattern, which does appear to have multiple cells radially as well as angularly.

Surface tension data on the SS 316L and 8630 heats has been presented by Sundell, *et al.* (Ref. 5). Their first-heat data of three heat/cool cycles were utilized here in a qualitative manner. This was believed to best represent the conditions of these single-cycle stationary welds. This is also a recommended source of surface tension data for use in theoretical models of these weld pools. It must be noted, however, that Ref. 5 data extend only over the limited range from approximately 1500° to 1900°C. Higher temperature surface tension data should be taken and made available to fully support and verify the analysis below.

Low-sulfur SS 316L (heats J and L) have $\partial\gamma/\partial T < 0$, and Type I-B or Type II-B weld pools would be expected. This is the case, as illustrated in Fig. 20B. For the SS 316L heat M, the high sulfur content tends to cause $\partial\gamma/\partial T$ to change from <0 to >0, and the surface tension and electromagnetic forces tend to reinforce each other. This results in a higher peak temperature with a Type I-A temperature profile. The 8630/3037 heat is high-purity low-cerium, silicon and sulfur. The surface tension gradient, $\partial\gamma/\partial T$, is >0. Thus a Type I-A temperature profile could be expected. Figure 20C shows that this is the case, having a characteristically high Type I-A central peak temperature. The 8630/3043 heat is high in cerium and is transi-

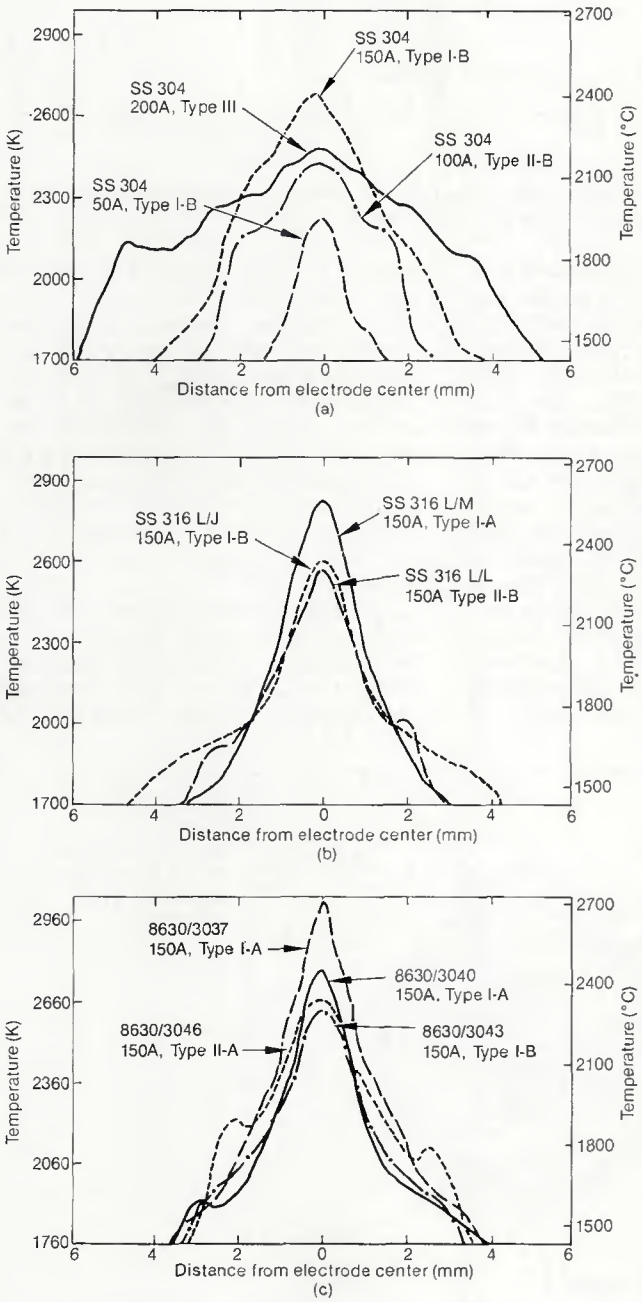

Fig. 20—Surface temperature profiles for SS 304, SS 316L, and 8630 weld pools taken from left to right through midpoint between the electrode and its spectral reflection in weld pool

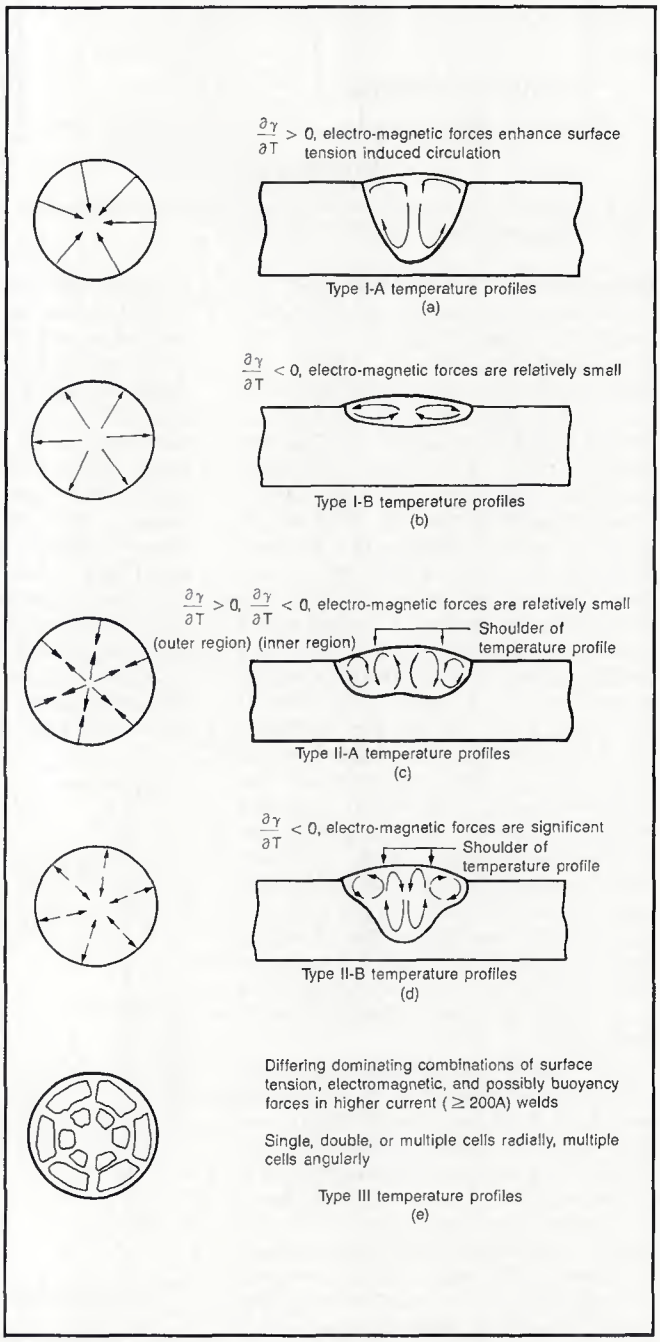

Fig. 21—Weld pool circulation patterns as related to surface temperature profile types

tional in nature with respect to surface tension dependence on temperature. Type II-A or reversion to Type I-B or II-B could be expected. A Type I-B temperature profile resulted for the 8630/3043, indicating that $\partial\gamma/\partial T < 0$ and that electromagnetic forces were insignificant relative to surface tension forces. The 8630/3040 is high in silicon and sulfur with $\partial\gamma/\partial T > 0$. A Type I-A temperature profile would be expected and was obtained as depicted in Fig. 20C. However, a small unexplained Type II shoulder is present on the left side of the profile. This may be a localized effect of transitional surface tension forces due to variation of sulfur or other surface active element concentrations in this region of the weld pool. Finally, for the 8630/3046 heat, which is high in cerium, silicon and sulfur, Ref. 5 data show $\partial\gamma/\partial T > 0$. Thus, a Type I-A temperature profile is most likely to occur. However, a Type II-A temperature profile, shown in Fig. 20C, actually occurred. Evidently, a transitional surface tension temperature exists for this 3046 heat for temperatures higher than those investigated in Ref. 5.

These temperature data are currently being used in a national laboratory cooperative effort for comparing thermal modeling results found using the WELDER program (Refs. 14, 17) to simulate these stationary welds. The actual specimens will be sectioned and analyzed for microstructure as part of this effort. The theoretical weld pool dome and workpiece penetration shapes will be compared to the actual measurements. The actual weld pool depth-to-width ratio will be discussed in the context of the previously observed effects of minor alloying elements and weld pool chemistry.

Conclusions

High-resolution molten pool surface temperatures have been obtained for stationary GTA welds on thick-plate SS 304, SS 316L and 8630 steels resulting in peak temperatures from ~2200 to 3000 K (~1950° to 2700°C). These temperatures generally increase for SS 304 with increasing welding current up to 150 A, but decrease when the welding current is further increased to 200 A. Resulting surface temperature profiles for all the alloys were classified into several types based on inferred weld pool convective flow patterns. The effect of minor alloying constituents on surface tension forces, which can dramatically affect weld pool shape and penetration as reported by previous researchers (Refs. 5, 7, 8), has been generally supported by these temperature results. However, a very complex surface temperature pattern results at a higher welding current of 200 A, believed to be indicative of a complex azimuthal-direction, multi-celled circulation pattern. This may be representative of the degree of complexity that occurs at higher welding currents, *i.e.*, over 150 A. Repeatability measurements were not performed here. However, past research (Refs. 3, 4) has shown that, for translating GTA welds made on thin-plate SS 304, weld pool surface temperature profiles do not reach absolute "quasi-steady-state" conditions. Rather, they typically vary 5 to 10% around some time-averaged or mean values. The temperature results presented in this article must therefore be labeled as representative only. Reference 4 research has also revealed that temperature results vary from welding machine to welding machine. Indeed, nearly any variation in the welding system parameters would likely result in different results, aside from the run-to-run variation expected. This would also include electrode tip angle, gas cup design, shielding gas flow, alloy heat, etc. One further conclusion, then, must be made. The optical spectral radiometric/laser reflectance system, developed as described here and in previous work (Refs. 1, 2), is a tool that must be applied to a particular system for weld pool surface temperature measurement. The data presented here and in other articles (Refs. 3, 4) are intended to aid in verification and further development of weld pool convection theories and overall welding process thermal models.

Acknowledgments

The author gratefully acknowledges H. B. Smartt for his continued support of this research effort in terms of laboratory space and equipment, and L. D. Reynolds for his assistance in the laboratory and in designing the coldplate. Thanks are expressed to T. W. Eagar of the Massachusetts Institute of Technology for making this author aware of the fast-shutoff capabilities of Astro Arc welding machines. Appreciation is expressed to R. E. Sundell of General Electric Co., Schenectady, N. Y., for providing samples of the SS 316L heats, and to D. W. Walsh of California Polytechnic Institute of Technology for providing the samples of the 8630 heats for this research. The author would also like to thank J. H. Carson, J. J. Guenette, R. Liljestrand and M. A. Lopez of EG&G Measurements, Los Alamos, N. Mex., for their aid in film processing, sensitometry, and imaging microdigitizing.

This research was funded by the Office of Naval Research under contract number N00014-85-F-0057. The author is employed at a Department of Energy research facility under contract number DE-AC07-76-ID01570.

References

1. Kraus, H. G. 1986. Optical spectral radiometric method for measurement of weld-pool surface temperatures. *Optics Letters* 11(12): 773-775.

2. Kraus, H. G. 1987. Optical spectral radiometric/laser reflectance method for noninvasive measurement of weld pool surface temperatures. *Opt. Eng.* 26(12):1183-1190.

3. Kraus, H. G. 1987. Experimental measurement of thin plate 304 stainless steel GTA weld pool surface temperatures. *Welding Journal* 66(12): 353-s to 359-s.

4. Kraus, H. G. 1989. Surface temperature measurements of GTA weld pools on thin plate SS 304. Published in *Welding Journal* 68(3): 84-s to 91-s.

5. Sundell, R. E., *et al.* 1986. *Minor Element Effects on Gas Tungsten Arc Weld Penetration.* Report No. 86SRD013 submitted to National Science Foundation, General Electric Company, Schenectady, N. Y.

6. Seigel, R., and Howell, J. R. 1976. *Thermal Radiation Heat Transfer,* 2nd Ed. McGraw-Hill.

7. Lin, M. L., and Eagar, T. W. 1985. Influence of arc pressure on weld pool geometry. *Welding Journal* 64(6):163-s to 169-s.

8. Schauer, D. A., Giedt, W. H., and Shintaku, S. M. 1978. Electron beam welding cavity temperature distributions in pure metals and alloys. *Welding Journal* 57(5):127-s to 133-s.

9. Giedt, W. H., Wei, X-C., and Wei, S.-R. 1984. Effect of surface convection on stationary GTA weld zone temperatures. *Welding Journal* 63(12): 376-s to 383-s.

10. Block-Bolton, A., and Eagar, T. W. 1984. Metal vaporization from weld pools. *Met. Trans. B* 15B(9):461-469.

11. Heiple, C. R., and Roper, J. R. 1982. Mechanism for minor element effect on GTA fusion zone geometry. *Welding Journal* 61(4):92-s to 102-s.

12. Heiple, C. R., Roper, J. R., and Aden, R. J. 1983. Surface active element effects on the shape of GTA, laser, and electron beam welds. *Welding Journal* 62(3):72-s to 77-s.

13. Burgardt, P., and Heiple, C. R. 1986. Interaction between impurities and welding variables in determining GTA weld shape. *Welding Journal* 65(6):150-s to 155-s.

14. Zacharia, T., Eraslan, A. H., Aidun, D. K., and David, S. A. 1989. Three-dimensional transient thermal model for arc welding processes. To be published.

15. Sahoo, P., Debroy, T., and McNallan, M. J. 1988. Surface tension of binary metal—surface active solute systems under conditions relevant to welding metallurgy. *Met. Trans. B* 19B(6):483-491.

16. Verlarde, M. G., and Normand, C. July 1980. Convection. *Scientific American:* 79-93.

17. Zacharia, T., Eraslan, A. H., and Aidun, D. K. 1988. Modeling of autogenous welding. *Welding Journal* 67(4): 53-s to 62-s.